INTERNATIONAL JOURNAL FOR NUMERICAL METHODS IN FLUIDS
Int. J. Numer. Meth. Fluids 2005; **48**:17–42
Published online 23 December 2004 in Wiley InterScience (www.interscience.wiley.com). DOI: 10.1002/fld.814

On Marangoni effects in a heated fluid layer with a monolayer surfactant. Part II: finite element formulation and numerical studies

Xiaowen Wang and Graham F. Carey*,†

The University of Texas at Austin, U.S.A.

SUMMARY

In this part we consider the dilute surfactant model developed in Part I and construct a variational formulation and mixed finite element scheme to obtain approximate solutions. In particular, we consider the stability regimes identified in the linear stability analysis of Part I and conduct numerical experiments to explore the nature of stability for the approximate solutions in these regimes. Both 1D and 2D simulation results are provided to illustrate the behaviour. Copyright © 2004 John Wiley & Sons, Ltd.

KEY WORDS: finite elements; surfactant and thermocapillary problem; Marangoni effects

1. INTRODUCTION

In Part I, we consider the Marangoni effect for long wavelength surface modes in coupled heat transfer with monolayer surfactant transport for a heated thin fluid layer. Scaling and perturbation analysis lead to a coupled non-linear transport system for the general surfactant model and a simpler (but still complicated) non-linear model for the case of dilute monolayer surfactants on the surface. A linear stability analysis is developed for this dilute model that leads to a categorization of the stability behaviour in terms of a pair of non-dimensional parameters ε_1 and D_s, where ε_1 is the non-dimensional stability control parameter and D_s is the inverse dynamic Bond number for solutocapillarity.

Here, we consider the coupled non-linear system for the dilute model and develop a mixed variational formulation of this fourth-order problem for construction of a corresponding finite element approximation model. Significant properties of the resulting semidiscrete finite element system are summarized. The solution algorithm is described and then implemented and applied in the final section to both 1D and 2D test problems to explore the non-linear stability regimes predicted by the linear stability analysis in Part I. In the 2D studies the ideas

*Correspondence to: Graham F. Carey, The University of Texas at Austin, U.S.A.
†E-mail: carey@cfdlab.ae.utexas.edu

Received 11 August 2003
Revised 18 October 2004

are also extended to explore the effect of the geometry of the container on the behaviour of the long wavelength oscillating elevation solution. Other details of the behaviour, such as the phase lag between the oscillations in elevation and oscillations in surfactant concentration on the surface, are also investigated numerically.

2. FINITE ELEMENT FORMULATION

In Section 2 of Part I, the governing equations for the long wavelength surface elevation and dilute surfactant concentration are derived, and expressed as follows:

$$\begin{aligned} \frac{\partial u}{\partial t} + \boldsymbol{\nabla}\cdot(a(u)\boldsymbol{\nabla}u + b(u)\boldsymbol{\nabla}\nabla^2 u) &= \boldsymbol{\nabla}\cdot(\kappa_u(u)\boldsymbol{\nabla}\Gamma) \\ \frac{\partial \Gamma}{\partial t} + \boldsymbol{\nabla}\cdot[\boldsymbol{C}(u)\Gamma] &= \boldsymbol{\nabla}\cdot(\kappa_\Gamma(u,\Gamma)\boldsymbol{\nabla}\Gamma) \end{aligned} \tag{1}$$

where u and Γ are the non-dimensional surface elevation and surfactant concentration, respectively,

$$\begin{aligned} a(u) &\equiv \frac{3}{2}\frac{D(1+F)u^2}{(1+F-Fu)^2} - u^3 \\ b(u) &\equiv \frac{u^3}{B} \\ \boldsymbol{C}(u) &\equiv \left(\frac{3D(1+F)u}{(1+F-Fu)^2} - \frac{3}{2}u^2\right)\boldsymbol{\nabla}u + \frac{3}{2}\frac{u^2}{B}\boldsymbol{\nabla}\nabla^2 u \\ \kappa_u(u) &\equiv \frac{3}{2}D_s u^2 \\ \kappa_\Gamma(u) &\equiv 3D_s u\Gamma \end{aligned} \tag{2}$$

and $B \equiv \rho g L^2/\sigma_{eq}^p$ is the static bond number, $F \equiv (d/d_g - H)/1 + H$ is the two-layer Biot number, $H \equiv k_g d/k d_g$ is the Biot number, $D = M/G = \sigma_T \Delta T^p/\rho g d^2$ is the inverse dynamic bond number, $D_s \equiv \alpha E \sigma_{eq}^p/\rho g d^2$ is the counterpart to D in the surfactant problem, $\alpha \equiv \Gamma_{eq}^p/\Gamma_\infty^p$ measures the fraction of interfacial area covered by surfactant, and $E \equiv RT^p\Gamma_\infty^p/\sigma_{eq}^p$ measures the sensitivity of surface tension to the local surfactant concentration. Here d and L are the average depth and horizontal extent of the thin fluid layer, ΔT^p is the temperature difference across the liquid layer, T^p is the temperature at the liquid–gas surface, g is the gravity acceleration, $\rho, \sigma, \nu, \kappa, k$, and k_g denote density, surface tension, kinematic viscosity and thermal diffusivity of the liquid, thermal conductivity of the liquid and the gas, respectively, $\sigma_T = -\partial\sigma/\partial T > 0$ is the thermocapillary coefficient, Γ_{eq}^p and Γ_∞^p are the surfactant concentrations at equilibrium and saturation state respectively, σ_{eq}^p is the surface tension at equilibrium state, and R is the ideal gas constant. (See part I and Reference [3] for further details).

Equation (1) introduces a new time dependent convection diffusion PDE for Γ in addition to the governing equation for the thermocapillary problem. Furthermore the governing equation

for elevation has an extra diffusion term involving Γ on the right-hand side. From the scaling analysis in Section 2.2 of Part I, we know that the convection velocity in the Γ equation is $O(1)$, so we can still apply a standard Galerkin type of formulation to the Γ equation without considering convective stability as long as the CFL number and cell Peclet number remain sufficiently small (mesh not too coarse).

Following a similar approach to that for the mixed formulation adopted in the surfactant-free problem of Reference [3], we get the mixed system formulation for (1)

$$\begin{aligned}
\frac{\mathrm{d}}{\mathrm{d}t}\int_\Omega uv\,\mathrm{d}\Omega &= \int_\Omega (a(u)\nabla u\cdot\nabla v + b(u)\nabla w\cdot\nabla v)\,\mathrm{d}\Omega - \int_\Omega \kappa_u(u)\nabla\Gamma\cdot\nabla v\,\mathrm{d}\Omega \\
&\quad - \oint_{\partial\Omega}\left(a(u)\frac{\partial u}{\partial n} + b(u)\frac{\partial w}{\partial n} - \kappa_u(u)\frac{\partial\Gamma}{\partial n}\right)v\,\mathrm{d}s \\
0 &= \int_\Omega (wq + \nabla u\cdot\nabla q)\,\mathrm{d}\Omega - \oint_{\partial\Omega}\frac{\partial u}{\partial n}q\,\mathrm{d}s \qquad (3)\\
\frac{\mathrm{d}}{\mathrm{d}t}\int_\Omega \Gamma\gamma\,\mathrm{d}\Omega &= \int_\Omega \Gamma\boldsymbol{C}(u)\cdot\nabla\gamma\,\mathrm{d}\Omega - \int_\Omega \kappa_\Gamma(u,\Gamma)\nabla\Gamma\cdot\nabla\gamma\,\mathrm{d}\Omega \\
&\quad - \oint_{\partial\Omega}\left(\Gamma\boldsymbol{C}(u)\cdot\boldsymbol{n} - \kappa_\Gamma(u,\Gamma)\frac{\partial\Gamma}{\partial n}\right)\gamma\,\mathrm{d}s
\end{aligned}$$

Note that the volume flux in the leading equation includes an extra term which comes from the surfactant-capillarity effect.

Using the same reasoning as in Reference [3], we specify the following natural boundary conditions:

$$\begin{gathered}
a(u)\frac{\partial u}{\partial n} + b(u)\frac{\partial w}{\partial n} - \kappa_u(u)\frac{\partial\Gamma}{\partial n} = 0 \\
\frac{\partial u}{\partial n} = 0 \qquad (4)\\
\Gamma\boldsymbol{C}(u)\cdot\boldsymbol{n} - \kappa_\Gamma(u,\Gamma)\frac{\partial\Gamma}{\partial n} = 0
\end{gathered}$$

to complete the finite element formulation. This choice of boundary conditions is globally volume conserving for u and mass conserving for Γ.

Introducing the approximation spaces U_h, W_h and G_h and replacing u, w and Γ in (3) with u_h, w_h, and Γ_h from these spaces, the mixed finite element approximation satisfies

$$\frac{\mathrm{d}}{\mathrm{d}t}\int_\Omega u_h v_h\,\mathrm{d}\Omega = \int_\Omega (a(u_h)\nabla u_h\cdot\nabla v_h + b(u_h)\nabla w_h\cdot\nabla v_h)\,\mathrm{d}\Omega$$

$$
\begin{aligned}
&- \int_\Omega \kappa_u(u_h)\nabla\Gamma_h \cdot \nabla v_h \, \mathrm{d}\Omega \\
0 &= \int_\Omega (w_h q_h + \nabla u_h \cdot \nabla q_h) \, \mathrm{d}\Omega \\
\frac{\mathrm{d}}{\mathrm{d}t} \int_\Omega \Gamma_h \gamma_h \, \mathrm{d}\Omega &= \int_\Omega \Gamma_h \boldsymbol{C}(u_h, w_h) \cdot \nabla \gamma_h \, \mathrm{d}\Omega - \int_\Omega \kappa_\Gamma(u_h, \Gamma_h)\nabla\Gamma_h \cdot \nabla\gamma_h \, \mathrm{d}\Omega
\end{aligned} \tag{5}
$$

for all admissible test functions.

In particular we use the familiar C^o Lagrange piecewise polynomial expansions

$$
u_h = \sum_j u_j \phi_j, \quad w_h = \sum_j w_j \psi_j, \quad \Gamma_h = \sum_j \Gamma_j \tau_j \tag{6}
$$

with test functions $v_h = \phi_i$, $q_h = \psi_i$, $\gamma_h = \tau_i$.

The resulting non-linear semidiscrete differential algebraic system for nodal vectors $(\boldsymbol{u}, \boldsymbol{w}, \boldsymbol{\Gamma})$ has the form

$$
\begin{aligned}
\boldsymbol{M}_{uu} \frac{\mathrm{d}\boldsymbol{u}}{\mathrm{d}t} &= \boldsymbol{K}_{uu}(\boldsymbol{u})\boldsymbol{u} + \boldsymbol{K}_{uw}(\boldsymbol{u})\boldsymbol{w} + \boldsymbol{K}_{u\Gamma}(\boldsymbol{u})\boldsymbol{\Gamma} \\
\boldsymbol{0} &= \boldsymbol{K}_{wu}\boldsymbol{u} + \boldsymbol{M}_{ww}\boldsymbol{w} \\
\boldsymbol{M}_{\Gamma\Gamma} \frac{\mathrm{d}\boldsymbol{\Gamma}}{\mathrm{d}t} &= (\boldsymbol{C}_{\Gamma u}(\boldsymbol{u}, \boldsymbol{w}) - \boldsymbol{K}_{\Gamma\Gamma}(\boldsymbol{u}, \boldsymbol{\Gamma}))\boldsymbol{\Gamma}
\end{aligned} \tag{7}
$$

where

$$
\begin{aligned}
\boldsymbol{M}_{uu} &= \left(\int \phi_i \phi_j \, \mathrm{d}\Omega \right) \\
\boldsymbol{K}_{uu}(\boldsymbol{u}) &= \left(\int a(u_h)\nabla\phi_i \cdot \nabla\phi_j \, \mathrm{d}\Omega \right) \\
\boldsymbol{K}_{uw}(\boldsymbol{u}) &= \left(\int b(u_h)\nabla\phi_i \cdot \nabla\psi_j \, \mathrm{d}\Omega \right) \\
\boldsymbol{K}_{u\Gamma}(\boldsymbol{u}) &= \left(\int \kappa_u(u_h)\nabla\phi_i \cdot \nabla\tau_j \, \mathrm{d}\Omega \right) \\
\boldsymbol{K}_{wu} &= \left(\int \nabla\psi_i \cdot \nabla\phi_j \, \mathrm{d}\Omega \right) \\
\boldsymbol{M}_{ww} &= \left(\int \psi_i \psi_j \, \mathrm{d}\Omega \right)
\end{aligned} \tag{8}
$$

$$\boldsymbol{M}_{\Gamma\Gamma} = \left(\int \tau_i \tau_j \, \mathrm{d}\Omega \right)$$

$$\boldsymbol{C}_{\Gamma u}(\boldsymbol{u}, \boldsymbol{w}) = \left(\int_{\Omega} [\alpha(u_h) \boldsymbol{\nabla} u_h + \beta(u_h) \boldsymbol{\nabla} w_h] \cdot \boldsymbol{\nabla} \tau_i \tau_j \, \mathrm{d}\Omega \right)$$

$$\boldsymbol{K}_{\Gamma\Gamma}(\boldsymbol{u}, \boldsymbol{\Gamma}) = \left(\int \kappa_{\Gamma}(u_h, \Gamma_h) \boldsymbol{\nabla} \tau_i \cdot \boldsymbol{\nabla} \tau_j \, \mathrm{d}\Omega \right)$$

$$\alpha(u) \equiv \frac{3D(1+F)u}{(1+F-Fu)^2} - \frac{3}{2}u^2$$

$$\beta(u) \equiv \frac{3}{2} \frac{u^2}{B}$$

The time discretization scheme used in the simulations described later is the familiar θ-method: At any time step (t_n, t_{n+1}) the coupled non-linear algebraic system with timestep parameter $0 \leqslant \theta \leqslant 1$

$$\begin{aligned} \boldsymbol{M}_{uu}\boldsymbol{u}^{n+1} - \theta \Delta t \boldsymbol{F}(\boldsymbol{u}^{n+1}, \boldsymbol{w}^{n+1}, \boldsymbol{\Gamma}^{n+1}) &= \boldsymbol{M}_{uu}\boldsymbol{u}^{n} + (1-\theta)\Delta t \boldsymbol{F}(\boldsymbol{u}^{n}, \boldsymbol{w}^{n}, \boldsymbol{\Gamma}^{n}) \\ \boldsymbol{M}_{ww}\boldsymbol{w}^{n+1} + \boldsymbol{K}_{wu}\boldsymbol{u}^{n+1} &= 0 \\ \boldsymbol{M}_{\Gamma\Gamma}\boldsymbol{\Gamma}^{n+1} - \theta \Delta t \boldsymbol{G}(\boldsymbol{u}^{n+1}, \boldsymbol{w}^{n+1}, \boldsymbol{\Gamma}^{n+1}) &= \boldsymbol{M}_{\Gamma\Gamma}\boldsymbol{\Gamma}^{n} + (1-\theta)\Delta t \boldsymbol{G}(\boldsymbol{u}^{n}, \boldsymbol{w}^{n}, \boldsymbol{\Gamma}^{n}) \end{aligned} \tag{9}$$

is solved, where

$$\begin{aligned} \boldsymbol{F}(\boldsymbol{u}, \boldsymbol{w}, \boldsymbol{\Gamma}) &\equiv \boldsymbol{K}_{uu}(\boldsymbol{u})\boldsymbol{u} + \boldsymbol{K}_{uw}(\boldsymbol{u})\boldsymbol{w} - \boldsymbol{K}_{u\Gamma}(\boldsymbol{u})\boldsymbol{\Gamma} \\ \boldsymbol{G}(\boldsymbol{u}, \boldsymbol{w}, \boldsymbol{\Gamma}) &\equiv (\boldsymbol{C}_{\Gamma u}(\boldsymbol{u}, \boldsymbol{w}) - \boldsymbol{K}_{\Gamma\Gamma}(\boldsymbol{u}, \boldsymbol{\Gamma}))\boldsymbol{\Gamma} \end{aligned} \tag{10}$$

In the present formulation, $\boldsymbol{w} = -\boldsymbol{M}_{ww}^{-1} K_{wu} \boldsymbol{u}$ is first used to eliminate $\boldsymbol{w}$ by substitution in the remaining equation. Then Newton iteration with a sparse direct solver for the linear Jacobian subsystems is applied to solve the reduced non-linear system:

$$\begin{aligned} \boldsymbol{M}_{uu}\boldsymbol{u}^{n+1} - \theta \Delta t \bar{\boldsymbol{F}}(\boldsymbol{u}^{n+1}, \boldsymbol{\Gamma}^{n+1}) &= \boldsymbol{M}_{uu}\boldsymbol{u}^{n} + (1-\theta)\Delta t \bar{\boldsymbol{F}}(\boldsymbol{u}^{n}, \boldsymbol{\Gamma}^{n}) \\ \boldsymbol{M}_{\Gamma\Gamma}\boldsymbol{\Gamma}^{n+1} - \theta \Delta t \bar{\boldsymbol{G}}(\boldsymbol{u}^{n+1}, \boldsymbol{\Gamma}^{n+1}) &= \boldsymbol{M}_{\Gamma\Gamma}\boldsymbol{\Gamma}^{n} + (1-\theta)\Delta t \bar{\boldsymbol{G}}(\boldsymbol{u}^{n}, \boldsymbol{\Gamma}^{n}) \end{aligned} \tag{11}$$

where

$$\begin{aligned} \bar{\boldsymbol{F}}(\boldsymbol{u}, \boldsymbol{\Gamma}) &\equiv \boldsymbol{F}(\boldsymbol{u}, -\boldsymbol{M}_{ww}^{-1}\boldsymbol{K}_{wu}\boldsymbol{u}, \boldsymbol{\Gamma}) \\ \bar{\boldsymbol{G}}(\boldsymbol{u}, \boldsymbol{\Gamma}) &\equiv \boldsymbol{G}(\boldsymbol{u}, -\boldsymbol{M}_{ww}^{-1}\boldsymbol{K}_{wu}\boldsymbol{u}, \boldsymbol{\Gamma}) \end{aligned} \tag{12}$$

Let superscript n denote the time step, and subscript k denote the iteration step. The corresponding Jacobian matrix at the current iteration within the timestep is

$$\boldsymbol{J}_k^n = \begin{bmatrix} \boldsymbol{M}_{uu} - \theta\Delta t \dfrac{\partial \bar{\boldsymbol{F}}(\boldsymbol{u}_k^n, \boldsymbol{\Gamma}_k^n)}{\partial \boldsymbol{u}} & -\theta\Delta t \dfrac{\partial \bar{\boldsymbol{F}}(\boldsymbol{u}_k^n, \boldsymbol{\Gamma}_k^n)}{\partial \boldsymbol{\Gamma}} \\ -\theta\Delta t \dfrac{\partial \bar{\boldsymbol{G}}(\boldsymbol{u}_k^n, \boldsymbol{\Gamma}_k^n)}{\partial \boldsymbol{u}} & \boldsymbol{M}_{\Gamma\Gamma} - \theta\Delta t \dfrac{\partial \bar{\boldsymbol{G}}(\boldsymbol{u}_k^n, \boldsymbol{\Gamma}_k^n)}{\partial \boldsymbol{\Gamma}} \end{bmatrix}$$

where

$$\begin{aligned}
\frac{\partial \bar{\boldsymbol{G}}(\boldsymbol{u},\boldsymbol{\Gamma})}{\partial \boldsymbol{u}} &= \frac{\mathrm{d}}{\mathrm{d}\boldsymbol{u}}(\boldsymbol{C}_{\Gamma u}(\boldsymbol{u})\boldsymbol{\Gamma}) - \frac{\mathrm{d}}{\mathrm{d}\boldsymbol{u}}(\boldsymbol{K}_{\Gamma\Gamma}(\boldsymbol{u},\boldsymbol{\Gamma})\boldsymbol{\Gamma}) \\
&= \left(\frac{\partial}{\partial u_j} \left\{ \left[\int_\Omega (\alpha(u)\nabla u + \beta(u)\nabla w)\cdot\nabla\tau_i\tau_k \,\mathrm{d}\Omega \right] \Gamma_k \right\} \right) \\
&\quad - \left(\frac{\partial}{\partial u_j} \left\{ \left[\int_\Omega \kappa_u(\boldsymbol{u},\boldsymbol{\Gamma})\nabla\tau_i\cdot\nabla\tau_k \,\mathrm{d}\Omega \right] \Gamma_k \right\} \right) \\
&= \boldsymbol{I}_1 + \boldsymbol{I}_2 + \boldsymbol{I}_3 + \boldsymbol{I}_4 - \boldsymbol{I}_5 \\
\boldsymbol{I}_1 &= \left(\int_\Omega \frac{\mathrm{d}\alpha(u_h)}{\mathrm{d}u}(\tau_k\Gamma_k)\nabla u\cdot\nabla\tau_i\phi_j \,\mathrm{d}\Omega \right) \\
\boldsymbol{I}_2 &= \left(\int_\Omega \alpha(u_h)(\tau_k\Gamma_k)\nabla\tau_i\cdot\nabla\phi_j \,\mathrm{d}\Omega \right) \\
\boldsymbol{I}_3 &= \left(\int_\Omega \frac{\mathrm{d}\beta(u_h)}{\mathrm{d}u}(\tau_k\Gamma_k)\nabla w\cdot\nabla\tau_i\phi_j \,\mathrm{d}\Omega \right) \\
\boldsymbol{I}_4 &= \left(\int_\Omega \beta(u_h)(\tau_k\Gamma_k)\frac{\partial\nabla w}{\partial u_j}\cdot\nabla\tau_i \,\mathrm{d}\Omega \right) \\
&= \left(\int_\Omega \beta(u_h)(\tau_k\Gamma_k)\nabla\psi_p\cdot\nabla\tau_i \,\mathrm{d}\Omega \right)(-\boldsymbol{M}_{ww}^{-1}\boldsymbol{K}_{wu}) \\
\boldsymbol{I}_5 &= \left(\int_\Omega \frac{\partial\kappa_{u\Gamma}(u_h,\Gamma_h)}{\partial u}(\nabla\tau_k\Gamma_k)\cdot\nabla\tau_i\phi_j \,\mathrm{d}\Omega \right) \\
\frac{\mathrm{d}\alpha(u)}{\mathrm{d}u} &= \frac{3D(1+F)(1+F+Fu)}{(1+F-Fu)^3} - 3u \\
\frac{\mathrm{d}\beta(u)}{\mathrm{d}u} &= \frac{3u}{B}
\end{aligned}$$

$$\frac{\partial \bar{\boldsymbol{G}}(\boldsymbol{u},\boldsymbol{\Gamma})}{\partial \boldsymbol{\Gamma}} = \boldsymbol{C}_{\Gamma u}(\boldsymbol{u}) - \boldsymbol{K}_{\Gamma\Gamma}(\boldsymbol{u},\boldsymbol{\Gamma}) - \left(\frac{\mathrm{d}\boldsymbol{K}_{\Gamma\Gamma}(\boldsymbol{u},\boldsymbol{\Gamma})}{\mathrm{d}\boldsymbol{\Gamma}}\right)\boldsymbol{\Gamma}$$

$$= \left(\int_{\Omega} [\alpha(u_h)\boldsymbol{\nabla} u_h + \beta(u_h)\boldsymbol{\nabla} w_h] \cdot \boldsymbol{\nabla}\tau_i \tau_j \,\mathrm{d}\Omega\right)$$

$$- \left(\int \kappa_{\Gamma}(u_h,\Gamma_h)\boldsymbol{\nabla}\tau_i \cdot \boldsymbol{\nabla}\tau_j \,\mathrm{d}\Omega\right)$$

$$- \left(\int \frac{\partial \kappa_{\Gamma}(u,\Gamma)}{\partial \Gamma}\tau_j \boldsymbol{\nabla}\tau_i \cdot (\boldsymbol{\nabla}\tau_k \Gamma_k)\,\mathrm{d}\Omega\right)$$

$$\frac{\partial \bar{\boldsymbol{F}}(\boldsymbol{u},\boldsymbol{\Gamma})}{\partial \boldsymbol{u}} = \boldsymbol{K}(\boldsymbol{u}) + \frac{\mathrm{d}\boldsymbol{K}(\boldsymbol{u})}{\mathrm{d}\boldsymbol{u}}\boldsymbol{u}$$

$$\boldsymbol{K}(\boldsymbol{u}) = \boldsymbol{K}_{uu}(\boldsymbol{u}) - \boldsymbol{K}_{uw}(\boldsymbol{u})\boldsymbol{M}_w^{-1}\boldsymbol{K}_{wu}$$

$$\frac{\mathrm{d}\boldsymbol{K}(\boldsymbol{u})}{\mathrm{d}\boldsymbol{u}}\boldsymbol{u} = \left(\frac{\partial (K)_{ik}}{\partial u_j}u_k\right)$$

$$= \left(\frac{\partial (K_{uu})_{ik}}{\partial u_j}u_k - \frac{\partial (K_{uw})_{ik}}{\partial u_j}(M_w^{-1}K_{wu})_{ks}u_s\right)$$

$$= \left(u_k \int \left.\frac{\mathrm{d}a(\eta)}{\mathrm{d}\eta}\right|_{\eta=\sum_t u_t\phi_t} \phi_j \nabla\phi_i \cdot \nabla\phi_k \,\mathrm{d}\Omega\right)$$

$$- \left(\int \left.\frac{\mathrm{d}b(\eta)}{\mathrm{d}\eta}\right|_{\eta=\sum_t u_t\phi_t} \phi_j \nabla\phi_i \cdot \nabla\psi_k \,\mathrm{d}\Omega (M_w^{-1}K_{wu})_{ks}u_s\right)$$

$$\frac{\mathrm{d}a(u)}{\mathrm{d}u} = 3u\left(\frac{D(1+F)^2}{(1+F-Fu)^3} - u\right)$$

$$\frac{\mathrm{d}b(u)}{\mathrm{d}u} = \frac{3u^2}{B}$$

$$\frac{\partial \bar{\boldsymbol{F}}(\boldsymbol{u},\boldsymbol{\Gamma})}{\partial \boldsymbol{\Gamma}} = -\boldsymbol{K}_{u\Gamma}(\boldsymbol{u}) = \left(\int \kappa_u(u_h)\boldsymbol{\nabla}\phi_i \cdot \boldsymbol{\nabla}\tau_j \,\mathrm{d}\Omega\right)$$

3. NUMERICAL STUDIES

3.1. Numerical results in 1D

In this section, several 1D numerical cases are first devised to display the behaviour in the different parametric regions of Figure 1 in a simple setting. The results are compared with

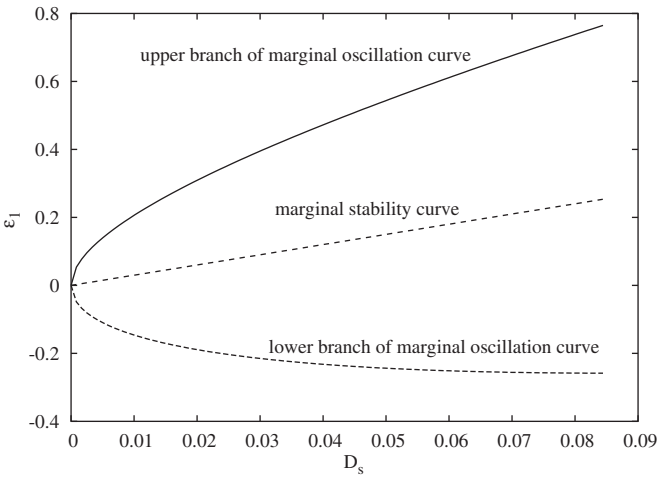

Figure 1. Marginal curves of ε_1 vs D_s.

analytical predictions based on the linear stability analysis. The following physical parameters apply to all the cases considered: $F = 0.85$, $B = 4\pi^2 \times 30$, $D_s = 0.042$. These F and B values are the same as adopted for the pure thermocapillary studies in Reference [3] and are based on VanHooks' experimental settings [2]. The D_s value is based on $E = 0.2$, which is used in Reference [5], and $\alpha = 2.5\%$, which is consistent with the dilute surfactant concentration assumption made in deriving the governing PDE (1) in Part I. The parameter to be varied is ε_1, which is chosen from different segments of the intersections of the marginal oscillation curve, the marginal stability curve, and the vertical line $D_s = 0.042$ presented in Figure 1.

Remark

Note that the D_s value here is based on the air–water system in Reference [6] whereas the F, B and ε_1 values are based on the air–silicone–oil system in Reference [2]. For an air–water system with DPPC as surfactant [6] at 20 °C, $k = 0.5984\,\mathrm{J/s \cdot m \cdot K}$, $\sigma_T = 1.7 \times 10^{-4}\,\mathrm{N/m \cdot K}$ [7], and $\sigma = 6.6 \times 10^{-2}\,\mathrm{N/m}$ [6]. The material properties of air remain the same. Thus with $d = 0.35\,\mathrm{mm}$, $d_g = 0.7\,\mathrm{mm}$, $L = 5\,\mathrm{cm}$, $\Delta T = 3.94°\mathrm{C}$, and $\alpha = 0.5\%$, we obtain the same D_s value: $D_s = 0.042$, and $\varepsilon_1 = 0.126$ is the same as used in case 2 in the next subsection. The B and F values are a little different from what are used here, though still typical of those used in VanHook's experiments: $B = 4\pi^2 \times 10^{\ddagger}$ and $F = 0.47$ Hence the results shown later are physically relevant for this class of problems.

If not stated otherwise, the numerical simulations use 100 uniform linear finite elements for all variables, $\theta = \frac{1}{2}$ in the time integration scheme, fixed time step size $\Delta t = 0.01$, Newton solve residual bound $1.0e-12$, and initial state $u(x, t = 0) = 1.0 + 0.05\cos(2\pi x)$, $\Gamma(x, t = 0) = 1$.

‡In VanHook' work [1] the horizontal domain span is normalized to $[0, 2\pi]$, whereas in this study it is normalized to [0,1]. Hence, B values in this study are $4\pi^2$ times of those in VanHook's work.

3.1.1. Oscillatory parameter region. We first consider the parameter region bounded by the upper and the lower branches of the marginal oscillation curve in Figure 1. As $(u(x,t),\Gamma(x,t))$ evolve in time, either damped or amplified oscillation are anticipated. Because the parameters are chosen such that all modes except for the leading one are stable and thus decay away, the analytical predictions are simply the results for the leading mode. The following are the theoretical predictions derived in Part I (see Section 3 of Part I for further details):

1. Oscillation period: $\tau = 1/\pi\sqrt{|\Delta_1|}$, $\Delta_1 = (\varepsilon_1 - 3D_s)^2 - 3D_s(1 + 4\pi^2/B)$.
2. Phase shift of Γ from u: $\phi = \tan^{-1}(\sqrt{|\Delta_1|}(3D_s + \varepsilon_1))$.
3. Exponential decay/growth rate of the amplitude of u and Γ: $\lambda = 2\pi^2(\varepsilon_1 - 3D_s)$.
4. Ratio of the amplitude of u vs that of Γ: $r = \sqrt{(1 + (\varepsilon_1/3D_s))^2 + (|\Delta_1|/9D_s^2)}$.

We shall see that standing waves are observed in all the cases in the oscillatory parameter region. Recall that in (33) and (34) of Part I u and Γ consist of a series of travelling wave pairs. If wave amplitudes $\eta_{q1} = \eta_{q2}$, then the qth pair of travelling waves add up to a standing wave. The reason for the consistent appearance of a standing wave in the numerical simulations is the choice of boundary conditions (4) used in the weak formulation (3). These are natural boundary conditions enforcing the volume flux of u and surface flux of Γ to be zero on the boundary, which requires the boundary flux due to the left-going wave balance that due to the right-going wave, essentially forcing them to have the same magnitude.

In the first numerical case, we specify $\varepsilon_1 = 0.1$. This falls in the parameter region between the lower branch of the marginal oscillation curve and the marginal stability curve in Figure 1. According to the linear stability analysis in Section 3 of part I, oscillatory decay of the initial perturbation is expected. The computed evolution history of the approximations $u_h(x,t)$ and $\Gamma_h(x,t)$ are shown in Figures 2 and 3. The evolution histories for the minimum and maximum values of u and Γ are shown in Figure 4. The attenuated oscillation in time is obvious from these two figures.

Remark

We can make some further observations on the qualitative behaviour of the solutions from Figures 2 and 3. The perturbation to u initially grows during the time interval $t = 0$–0.15 because $\varepsilon_1 > 0$. In the surfactant-free thermocapillary problem this would be an unstable case, and since $\mathrm{d}\Gamma/\mathrm{d}x = 0$ at $t = 0$, there is little contribution from surfactant to the surface tension gradient initially. The outgoing flow induced by the perturbation on u advects surfactant towards the ends, as shown by $\Gamma(x, t = 0.15)$. This, in turn, leads to an increase of surface tension in the centre and thus pulls the fluid back towards the centre, as shown by $u(x, t = 0.29)$ and $u(x, t = 0.43)$. The changes in the elevation u then affect the advection of Γ and the profile of Γ almost levels out at around $t = 0.43$. This competition continues throughout the solution evolution and gives rise to the cyclic behaviour of u and Γ. Clearly a phase difference between the elevation and the concentration is present.

In the second case, we specify $\varepsilon_1 = 3D_s = 0.126$. From linear stability analysis, oscillation in time with no amplitude attenuation is expected for this parameter choice. This can be visually confirmed from the evolution histories of $u(x,t)$, $\Gamma(x,t)$ [4], and their minimum and maximum values shown in Figure 5.

In the third case, the parameter region between the upper branch of the marginal oscillation curve and the marginal stability curve is studied. Based on the linear stability analysis

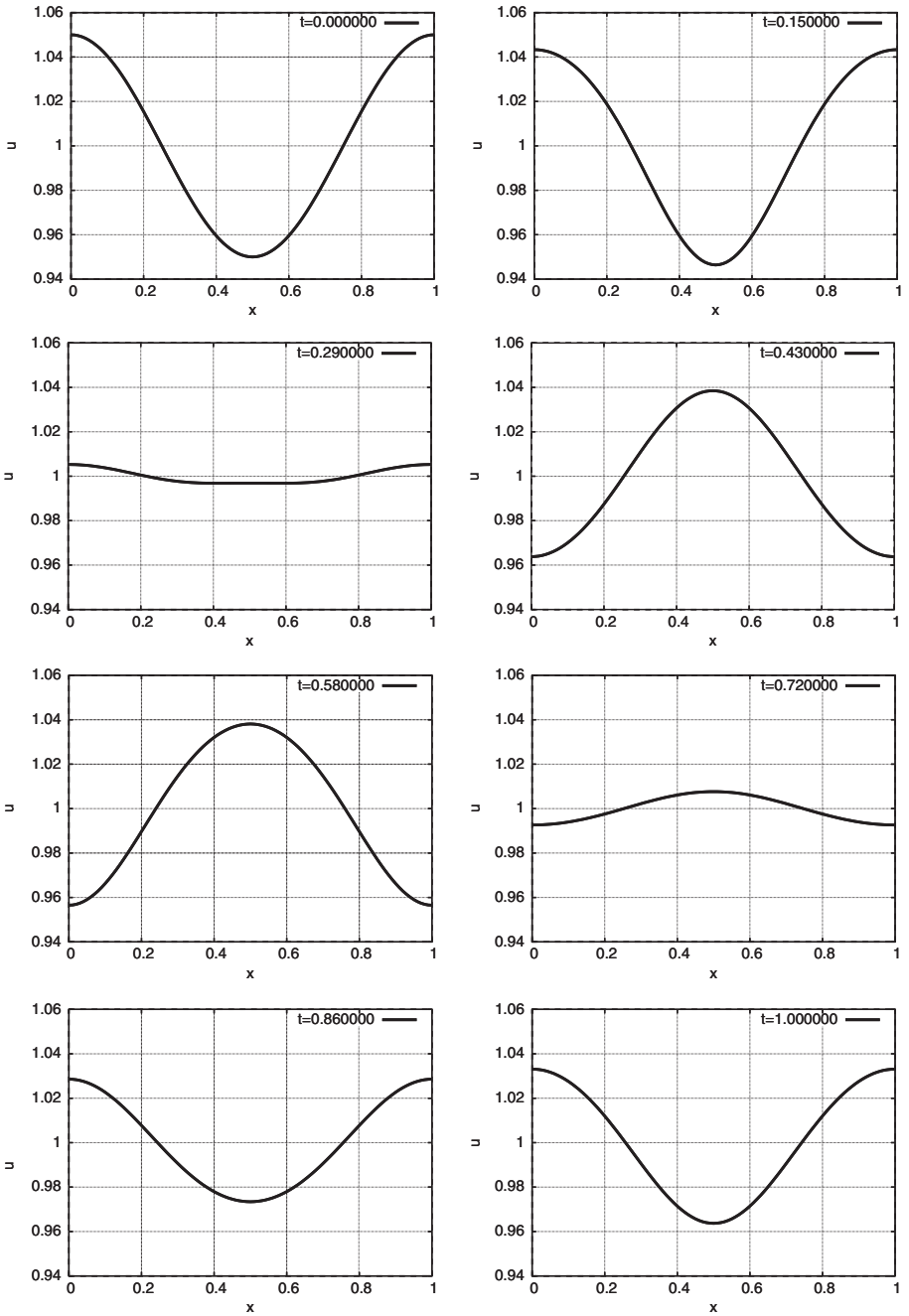

Figure 2. $u(x,t)$. $\varepsilon_1 = 0.1$, $D_s = 0.042$, $B = 4\pi^2 \times 30$. Attenuated oscillation.

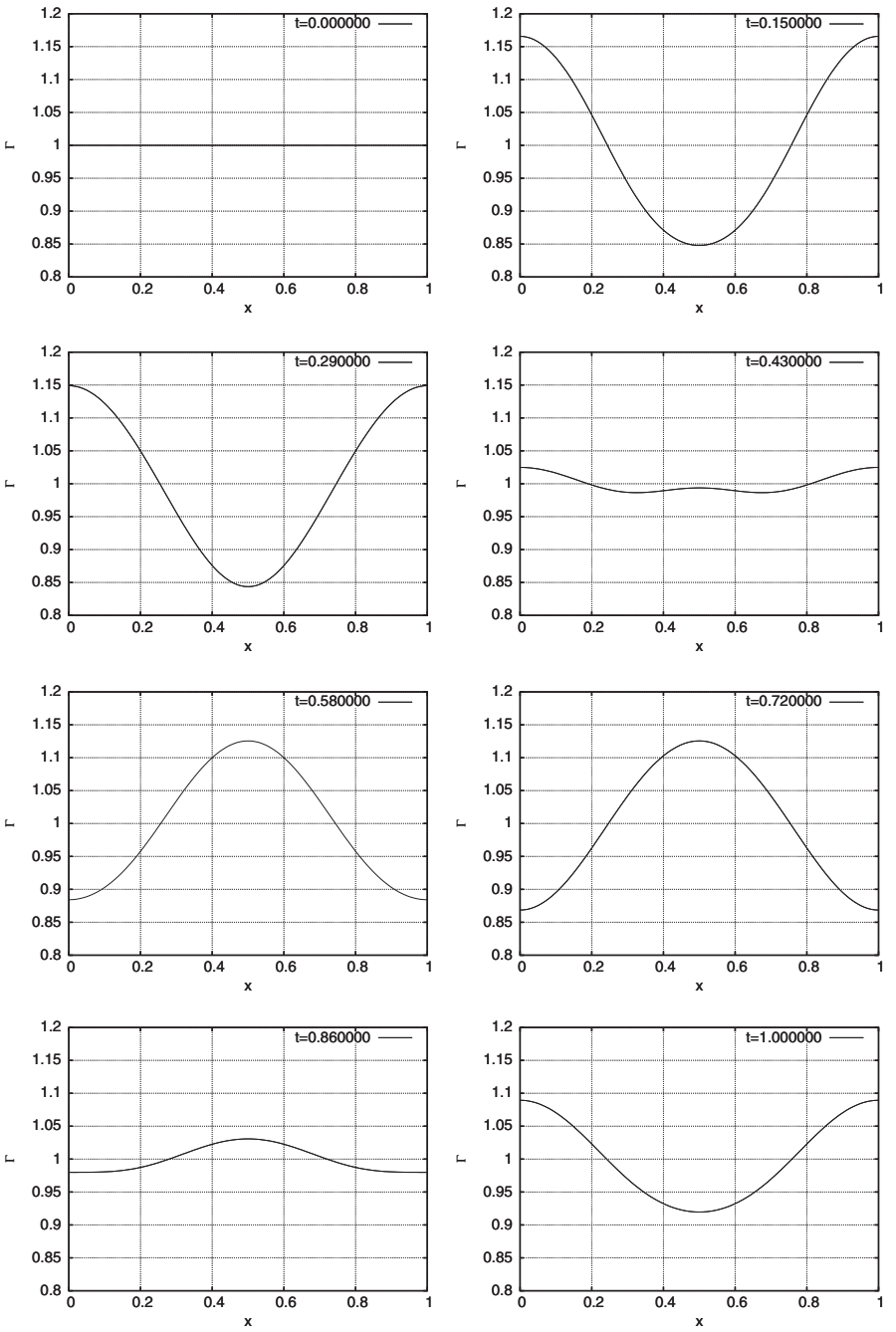

Figure 3. $\Gamma(x,t)$. $\varepsilon_1 = 0.1$, $D_s = 0.042$, $B = 4\pi^2 \times 30$. Attenuated oscillation.

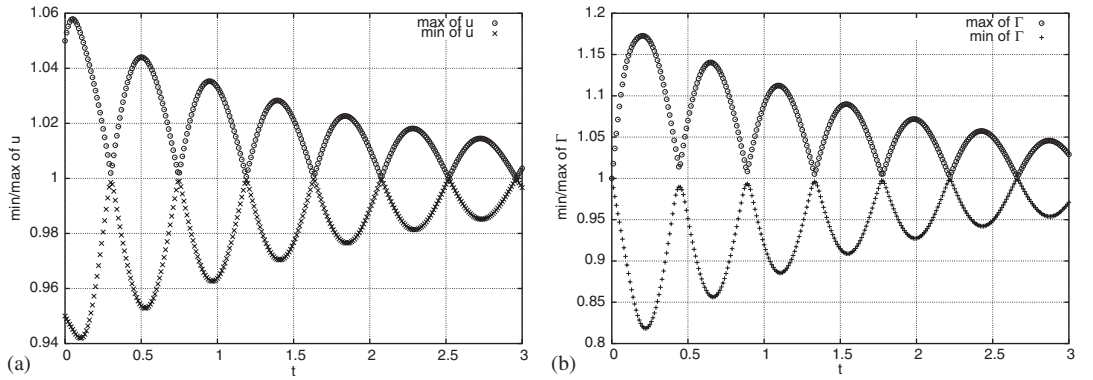

Figure 4. min/max values of u and Γ vs time. $\varepsilon_1 = 0.1$, $D_s = 0.042$, $B = 4\pi^2 \times 30$. Attenuated oscillation: (a) min/max of u; and (b) min/max of Γ.

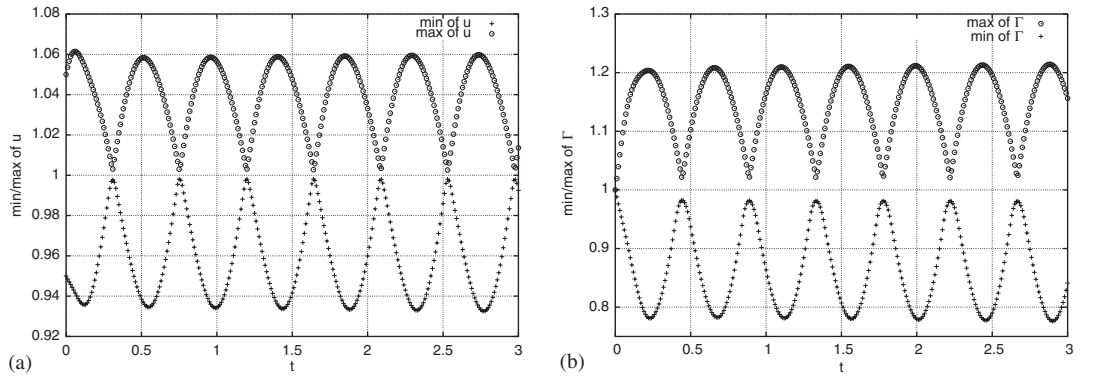

Figure 5. min/max values of u and Γ vs time. $\varepsilon_1 = 0.126$, $D_s = 0.042$, $B = 4\pi^2 \times 30$. Unattenuated oscillation: (a) min/max of u; and (b) min/max of Γ.

in Part I, oscillatory growth of the initial perturbation is expected. Because it is difficult to attain convergence in the non-linear solver when integrating an unstable evolution system with an implicit scheme, a marginally unstable case $\varepsilon_1 = 0.15$ is chosen here and a smaller time step $\Delta t = 0.0025$ is used to help the convergence of the non-linear solution. The evolution histories of $u(x,t)$, $\Gamma(x,t)$ [4], and their minimum and maximum values on the grid points are shown in Figure 6.

Table I shows the analytical predictions, the corresponding quantities calculated from the numerical results, and their relative difference for the oscillatory cases discussed in this section. The calculated quantities are obtained as follows: first extract the peak values of $\max_{x_i} u - 1$, $\max_{x_i} \Gamma - 1$, $1 - \min_{x_i} u$ and $1 - \min_{x_i} \Gamma$, and the corresponding times; then use these sequences to obtain the mean values and standard deviations; finally combine the values obtained from these four sequences to come up with the mean and deviation. It is evident that the corresponding analytical predictions and numerical quantities agree with each other within a few percent.

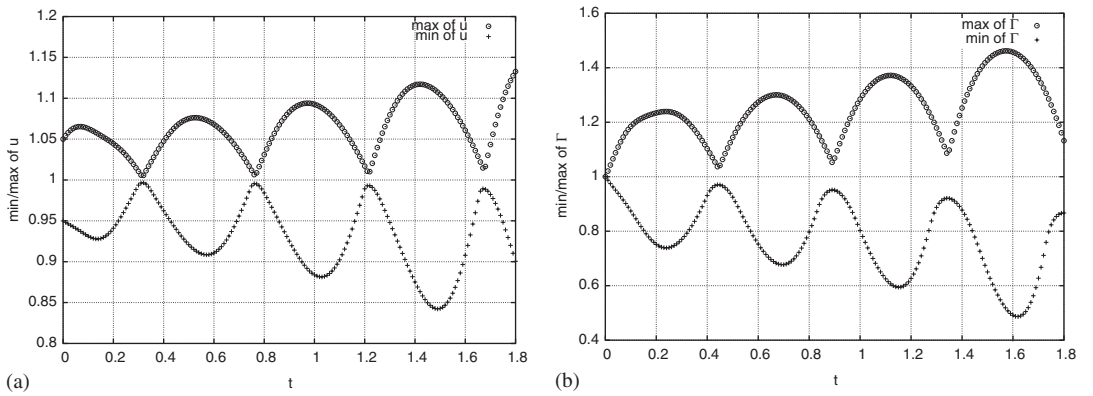

Figure 6. min/max values of u and Γ vs time. $\varepsilon_1 = 0.15$, $D_s = 0.042$, $B = 4\pi^2 \times 30$. Amplified oscillation: (a) min/max of u; and (b) min/max of Γ.

Table I. Comparison of analytical predictions and values post-processed from numerical results.

Numerical case	Case 1	Case 2	Case 3
ε_1	0.1	0.126	0.15
D_s	0.042	0.042	0.042
Oscillation period τ			
τ_{theo}	0.88445	0.88215	0.88411
τ_{num}	0.88585 ± 0.0094031	0.88833 ± 0.011666	0.90333 ± 0.017608
δ_τ	0.15829%	0.69716%	2.1739%
Phase shift ϕ			
ϕ_{theo}	57.873°	55.070°	52.526°
ϕ_{num}	$57.186° \pm 2.6849°$	$55.578° \pm 3.0634°$	54.299 ± 4.7701
δ_ϕ	1.1871%	0.92246%	3.3755%
Exponential rate λ			
λ_{theo}	−0.51322	0	0.47347
λ_{num}	-0.51443 ± 0.0089182	0.010023	0.49822 ± 0.058969
δ_λ	0.23577%	N/A	5.2296%
Amplitude ratio r			
r_{theo}	3.3728	3.4930	3.6004
r_{num}	3.1187 ± 0.026076	3.4324 ± 0.029116	3.6411 ± 0.069295
δ_r	7.5338%	1.7349%	1.1304%

Subscript theo means theoretical value from linear stability analysis, subscript num means numerical value from simulation, and δ_X means relative difference between theoretical and numerical values of parameter X in percent.

Remark

In most of the profile envelope history plots of u and Γ, i.e. the plots of the min/max values of u and Γ vs time, the separation between the max and min curves is not zero. Both curves approach unity but do not touch. In Reference [4] we consider case 2, and plot u and Γ at

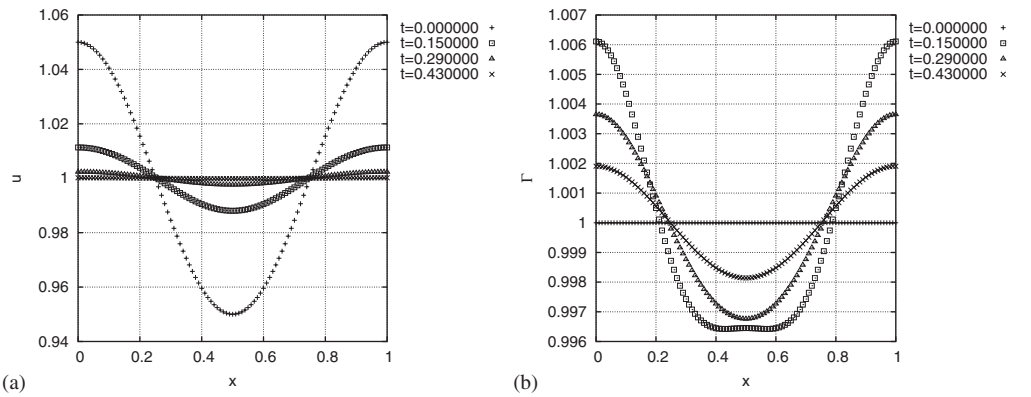

Figure 7. $u(x,t)$ and $\Gamma(x,t)$. $\varepsilon_1 = -0.23483$, $D_s = 0.042$, $B = 4\pi^2 \times 30$. Marginal non-oscillatory: (a) evolution of u; and (b) evolution of Γ.

three nearby time steps to confirm the separation is not zero, and that the positions of the min/max values are changing over time.

3.1.2. Non-oscillatory parameter region. In this subsection, the parameter region exterior to the marginal oscillation curve is studied. As $u(x,t)$ and $\Gamma(x,t)$ evolve in time, non-periodic decay or amplification of the initial perturbation is expected. Above the upper branch of the marginal oscillation curve, ε_1 is positive and has a large magnitude, and as a consequence numerical integration with an implicit scheme cannot proceed to the point where meaningful computations can be made without divergence in the Newton solver. Therefore, only the parameter region below the lower branch of the marginal oscillation curve is studied. Because the parameters are chosen such that all modes except for the leading one will decay, the analytical predictions are again the results for the leading mode:

1. The exponential growth rate: $\lambda = 2\pi^2(\varepsilon_1 - 3D_s \pm \sqrt{\Delta_1})$.
2. The ratio of the amplitude of u vs that of Γ: $r = 1 + (\varepsilon_1/3D_s) \mp (\sqrt{\Delta_1}/3D_s)$.

We compare both exponential growth rates with the numerical results. However, because the decay of the component of the faster rate is accompanied by a significant amount of the component of the slower rate, the calculation of the faster rate may not be as accurate as the slower rate.

First the special case where (ε_1, D_s) is on the lower branch of the marginal oscillation curve is studied. In this case $\varepsilon_1 = 3D_s - \sqrt{3D_s(1 + (4\pi^2/B))} = -0.23483$. According to the linear stability analysis, no oscillation is expected, and the initial perturbation should decay. Figure 7 shows the evolution of u and Γ. Figure 8 shows the evolution of the amplitudes for the perturbations of u and Γ. Note the dip in the $\max_{x_i} u - \min_{x_i} u$ plot at around $t = 0.47$. Figure 9 zooms in on this time interval and shows that there is a 'flip' in the profile of $u(x,t)$, during this time and this is consistent with the trend observed from the solutions in the oscillatory parameter region. This confirms that the dip in the decay of the amplitude of $u(x,t)$ is caused by the remaining weak oscillation in the solution.

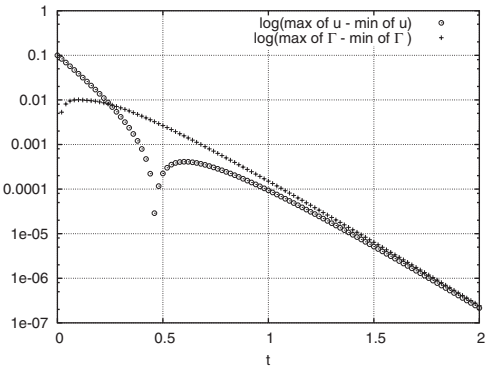

Figure 8. Semilog plot of $\max_{x_i} u(x,t) - \min_{x_i} u(x,t)$ vs time and $\max_{x_i} \Gamma(x,t) - \min_{x_i} \Gamma(x,t)$ vs time. $\varepsilon_1 = -0.23483$, $D_s = 0.042$, $B = 4\pi^2 \times 30$. Marginal non-oscillatory.

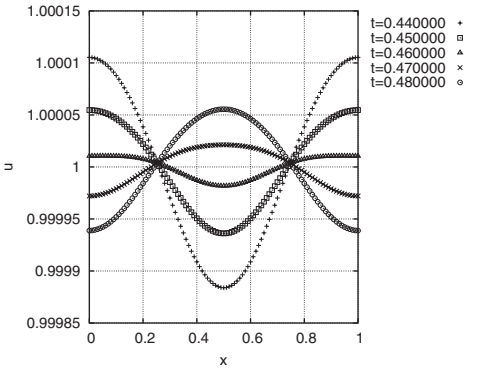

Figure 9. The flip of $u(x,t)$ profile in $t = 0.46$–0.47. (ε_1, D_s) is on the lower branch of the marginal oscillation curve.

With some experimenting, if ε_1 is decreased to $\varepsilon_1 = -0.26$, that is, if (ε_1, D_s) is pushed further below the marginal oscillation curve, the dip in the semilog plot of $\max_{x_i} u(x,t) - \min_{x_i} u(x,t)$ disappears. There is no significant change to the evolution of u, but the profile of Γ as shown in Figure 10 is significantly different from that shown in Figure 7. It behaves as if the surfactant-capillarity effect becomes much stronger when $\varepsilon_1 = -0.26$ so that it is able to pull up the Γ profile well above $\Gamma = 1$ in the middle region during the initial transient phase, whereas when $\varepsilon = -0.23483$, this pull-up just barely takes place. Figure 11 shows the history of the magnitude of the perturbations to u and Γ. It is observed that during $t \sim [0.2, 0.3]$ and after around $t = 1.5$, both u and Γ follow the same exponential decay.

If ε_1 is reduced, thermo-capillarity is weakened compared to surfactant-capillarity. Continuing this procedure, we reach a special case when the thermocapillarity is completely turned off, where the system is only subject to surfactant-capillarity, gravity and surface tension. This

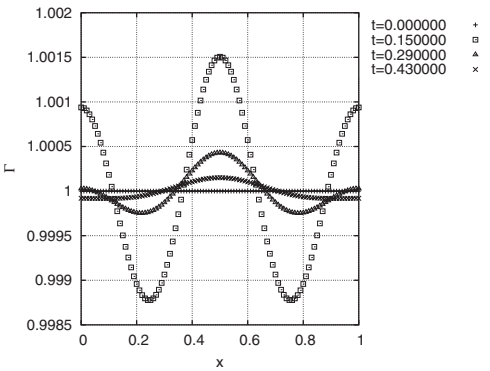

Figure 10. $\Gamma(x,t)$. $\varepsilon_1 = -0.26$, $D_s = 0.042$, $B = 4\pi^2 \times 30$. Diffusive decay.

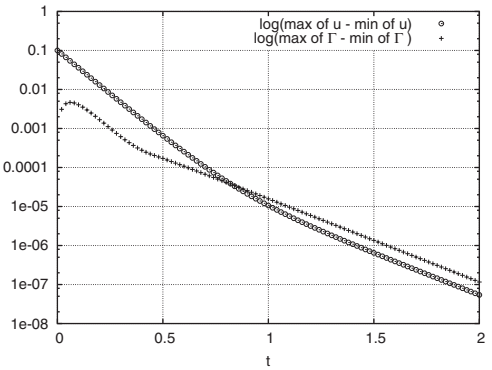

Figure 11. Semilog plot of $\max_{x_i} u(x,t) - \min_{x_i} u(x,t)$ vs time and $\max_{x_i} \Gamma(x,t) - \min_{x_i} \Gamma(x,t)$ vs time. $\varepsilon_1 = -0.26$, $D_s = 0.042$, $B = 4\pi^2 \times 30$. Diffusive decay.

can be realized by setting $\Delta T = 0$ so that $D = 0$. Thus

$$\varepsilon_q = -\left(1 + \frac{4\pi^2 q^2}{B}\right) < 3D_s - \sqrt{3D_s\left(1 + \frac{4\pi^2 q^2}{B}\right)}$$

which means (ε_1, D_s) is below the lower branch of the marginal oscillation curve when $D = 0$. Therefore, with the thermocapillarity turned off, the system should be stable. Figure 12 shows the evolution of the amplitudes for this case. Further details are also given in Reference [4].

Tables II and III show the analytical predictions, the corresponding quantities post-processed from the numerical results, and their relative difference for the longer and shorter exponential rates, respectively. The procedure to compute these quantities is the same as described earlier in the oscillatory case, except that here the quantities are computed from only the part of the history in which the scale to be calculated is believed to dominate. The notations used in these tables are the same as those in Table I.

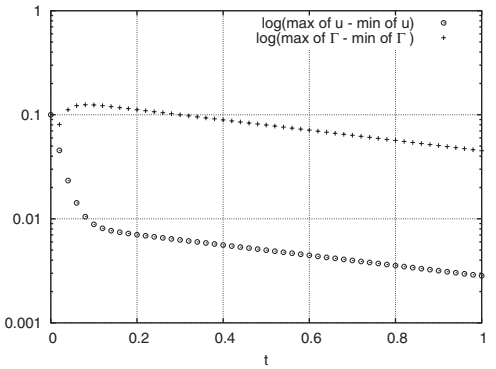

Figure 12. Semilog plot of $\max_{x_i} u(x,t) - \min_{x_i} u(x,t)$ vs time and $\max_{x_i} \Gamma(x,t) - \min_{x_i} \Gamma(x,t)$ vs time. $\varepsilon_1 = -1.0333$, $D_s = 0.042$, $B = 4\pi^2 \times 30$, $D = 0$.

Table II. Comparison of analytical predictions of the LONGER time scale component with the values post-processed from the numerical results.

Numerical case	Case 1	Case 2	Case 3
ε_1	-0.23483	-0.26	-1.0333
D_s	0.042	0.042	0.042
Exponential rate λ_1			
λ_{theo}	-7.1225	-4.9131	-1.1367
λ_{num}	-6.4436 ± 0.15008	-4.9377 ± 0.036122	-1.1362 ± 0.00057994
δ_λ	9.4967%	0.5007%	0.043987%
Amplitude ratio r_1			
r_{theo}	0.86379	2.1516, 0.024591	15.945, 1.5430
r_{num}	1.1810 ± 0.038292	2.1285 ± 0.017394	15.943 ± 0.0061340
δ_r	36.723%	1.0736%	0.012543%

Calculations are based on the evolution history after the initial transient phase.

From Table II, it is clear that in cases 2 and 3 we get good agreement between the analytical predictions and the values post-processed from the numerical results, whereas in case 1 the differences are more pronounced. We believe this is because in case 1 (ε_1, D_s) is right on the marginal oscillation curve so its behaviour is borderline between those in the non-oscillatory region and those in the oscillatory region.

Examining Table III, the difference between the analytical predictions and the values post-processed from the numerical results is more pronounced than in Table II. This is because the numerical results used in Table III include the initial phase, during which the components of the faster and slower exponential rates coexist, whereas in Table II the numerical results are for the later phase, during which only the component of the slower rate is significant. Also note that the amplitude ratio in Table III is quantitatively far from the analytical predictions. In case 3 the amplitude ratio cannot even be calculated from the numerical results because we cannot find a time interval in which the faster decaying components of u and Γ are both in the exponential decay phase. We believe this is due to the initial transient phase necessary

Table III. Comparison of analytical predictions of the SHORTER time scale component with the values post-processed from the numerical results.

Numerical case	Case 2	Case 3
ε_1	-0.26	-1.0333
D_s	0.042	0.042
Exponential rate λ_2		
λ_{theo}	-10.326	-44.631
λ_{num}	-10.116 ± 0.032	-39.4
δ_λ	2.033%	11.72%
Amplitude ratio r_2		
r_{theo}	0.024591	1.5430
r_{num}	0.12967 ± 0.000337	N/A
δ_r	437%	N/A

Values for case 2 are computed on $t = 0.2$–0.3, values for case 3 are computed on $t = 0$–0.03. The amplitude ratio in case 3 cannot be computed because Γ has not gone through the transient phase in the relevant time frame. The exponential rate in case 3 is computed from u only because Γ does not depict the exponential decay at the shorter time scale in this case.

for Γ to evolve from a flat profile to a profile compatible with u as predicted by the linear stability analysis. Nevertheless, the numerical results do capture the qualitative, and in many cases quantitative, behaviour of the system in the non-oscillatory parameter region.

For the special case where $D_s = 0$, we set $\varepsilon_1 = -0.1$ so that u eventually approaches the flat profile $u = 1$. As explained in the previous section, the perturbation to Γ will decay as well. However, the final Γ profile is not flat since it is determined by the evolution history of u.

3.2. Numerical results in 2D

We first conduct numerical experiments on the unit square for cases with parameters chosen in the oscillatory and non-oscillatory parameter regions. The results are compared with the estimates from linear stability analysis. We then study the evolution of surface elevation and surfactant concentration for other geometries. Unless mentioned otherwise, we employ the same finite element formulation, physical parameter values, time integration scheme and non-linear solver setting as used in the 1D study.

The first case is devised to validate against the linear stability analysis in the oscillatory parameter region. The domain is the unit square $x, y \in [0,1] \times [0,1]$. The initial state is $u(x, y, t=0) = 1 + 0.05\cos(2\pi x)\cos(2\pi y)$. The perturbation has a wave number of $q = \sqrt{q_x^2 + q_y^2} = \sqrt{2}$. If we let $\varepsilon_{\sqrt{2}} = 3D_s$, then from Part I we know that this case falls in the oscillatory parameter region and we expect the wave amplitude will stay unchanged. Figures 13 and 14 show that u and Γ evolve like standing waves with the amplitudes unchanged. Figure 15 plots the minimum and maximum values of $u(x, y, t)$ and $\Gamma(x, y, t)$ vs t and Table IV compares the analytical results with the values post-processed from the numerical results. The agreement is reasonably good, except for the phase angle. We suspect this discrepancy is still due to the initial transient phase needed for Γ to catch up.

The second case is devised to validate against the linear stability analysis in the non-oscillatory parameter region. The setting is the same as in the second case, except that

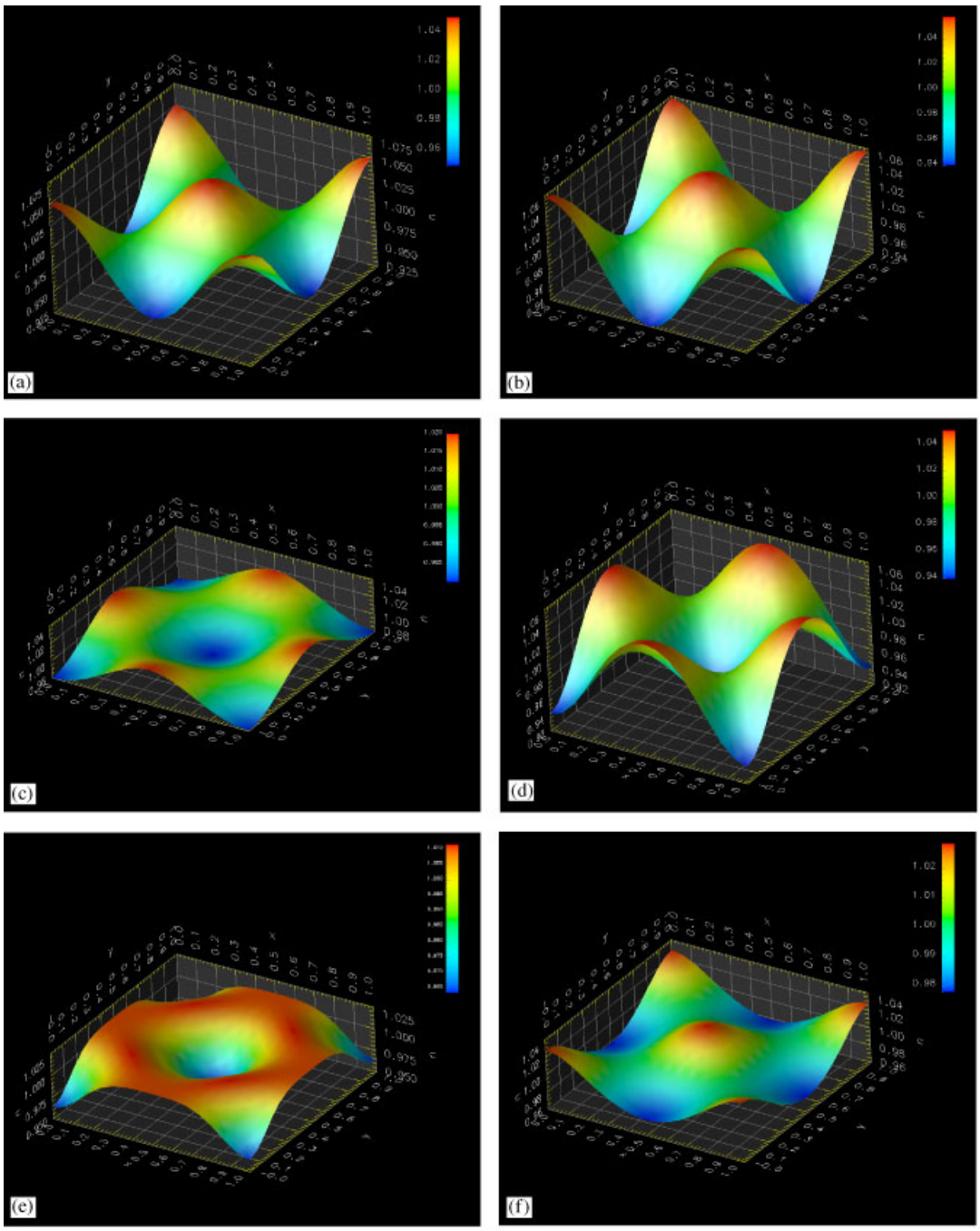

Figure 13. $u(x, y, t)$. $\varepsilon_{\sqrt{2}} = 3D_s = 0.126$. $\Delta t = 0.001$, $T = 1$: (a) u at $t = 0$; (b) u at $t = 0.06$; (c) u at $t = 0.175$; (d) u at $t = 0.29$; (e) u at $t = 0.345$; and (f) u at $t = 0.4$.

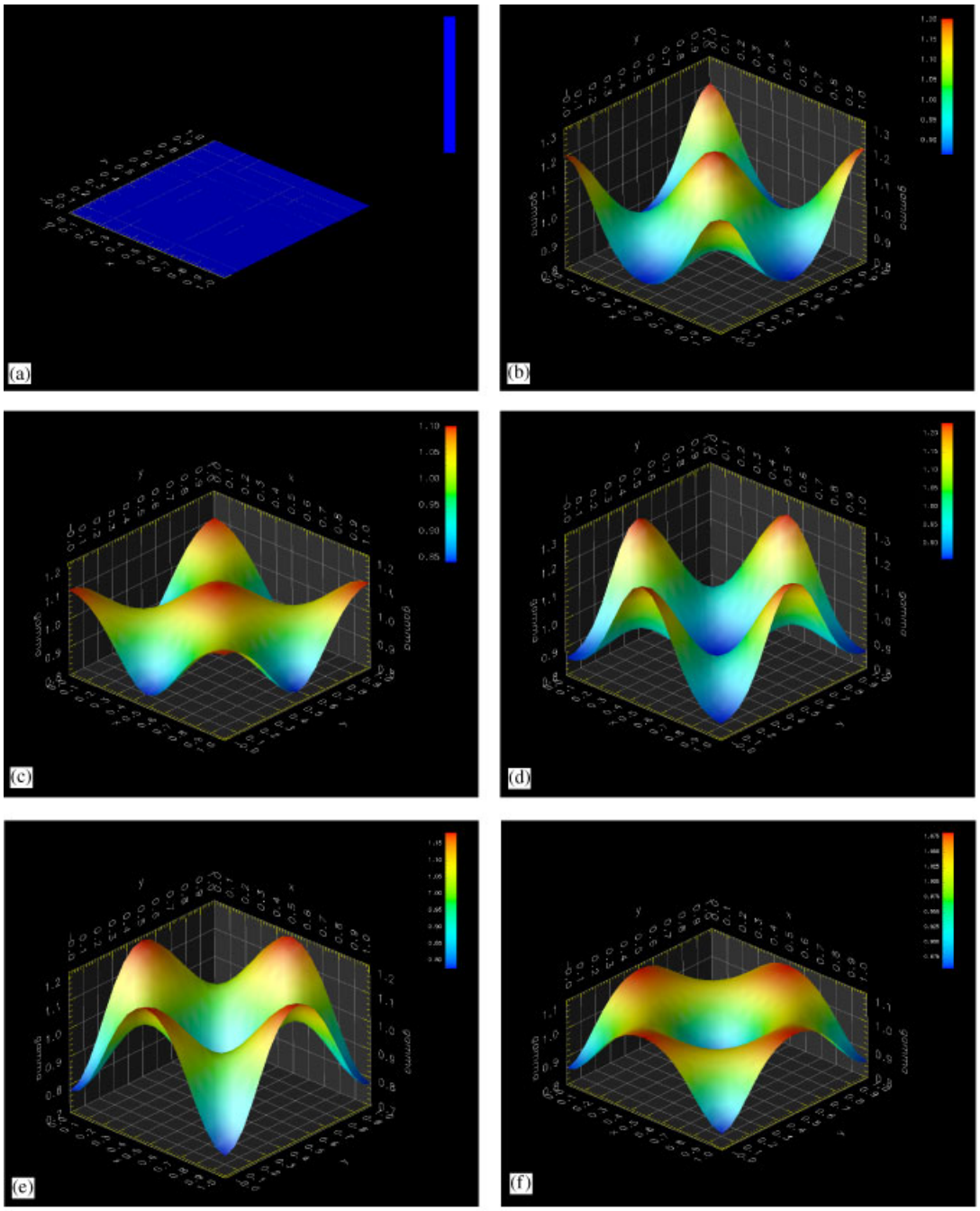

Figure 14. $\Gamma(x, y, t)$. $\varepsilon_{\sqrt{2}} = 3D_s = 0.126$. $\Delta t = 0.001$, $T = 1$: (a) $\Gamma = 1$ at $t = 0$; (b) Γ at $t = 0.06$; and (c) Γ at $t = 0.175$; (d) Γ at $t = 0.29$; (e) Γ at $t = 0.345$; and (f) Γ at $t = 0.4$.

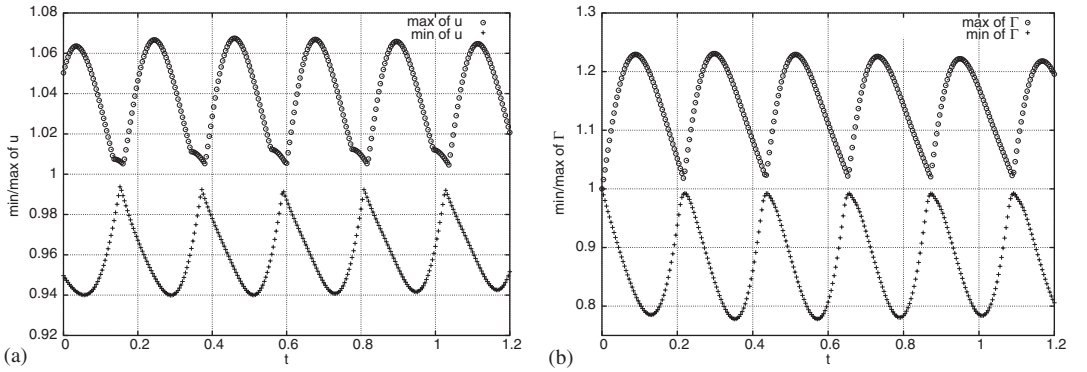

Figure 15. Min/max of $u(x, y, t)$ and $\Gamma(x, y, t)$ vs t. $\varepsilon_{\sqrt{2}} = 3D_s = 0.126$. $\Delta t = 0.001$, $T = 1$: (a) min/max of u; and (b) min/max of Γ.

Table IV. Comparison of analytical predictions with values post-processed from numerical experiments. $\varepsilon_{\sqrt{2}} = 3D_s = 0.126$. $\Delta t = 0.001$, $T = 1$.

	Analytical	Numerical	Relative difference
Period τ	0.43413	0.4365 ± 0.0087	0.546%
Exponential rate λ	0	-0.0086 ± 0.033	N/A
Phase shift ϕ	$-55.496°$	-48.66 ± 2.7916	12.32%
Amplitude ratio r	3.5307	3.5542 ± 0.0302	0.918%

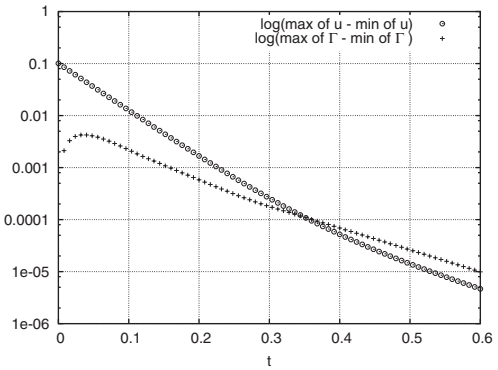

Figure 16. Min/max of $u(x, y, t)$ and $\Gamma(x, y, t)$ vs t. $\varepsilon_{\sqrt{2}} = -0.27$. $\Delta t = 0.001$, $T = 0.6$.

$\varepsilon_{\sqrt{2}} = -0.27$ (Figure 16), which is below the lower branch of the marginal oscillation curve. This is the counterpart to case 2 in the previous section on 1D results. As in 1D, the perturbation of u decays monotonically, whereas Γ first quickly grows to an amplitude that is compatible with u, and then starts to decay monotonically. For $t \in (0, 0.1)$, the exponential

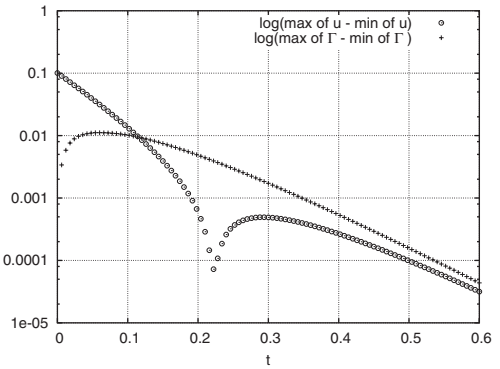

Figure 17. History of amplitudes of $u(x, y, t)$ and $\Gamma(x, y, t)$. $\varepsilon_{\sqrt{2}} = 3D_s - \sqrt{3D_s(1 + 4\pi^2 \times 2/B)}$. $\Delta t = 0.001$, $T = 0.6$.

rate of the short time scale component is least-square fit to be -20.786. This differs by 3.52% from the analytical prediction of -21.544, which is a fair agreement. For $t \in (0.55, 0.6)$, the long time scale component is least-square fit to be -10.75, which has a rather large 10.57% difference from the analytical prediction of -9.7228.

Recall that in case 1 of the study in 1D for the non-oscillatory parameter region, we observed a dip in the amplitude history of u for (ε_1, D_s) on the lower branch of the marginal oscillation curve of the leading mode. Zooming in on the neighbouring time interval indicates that there is a slight flip in the profile of u that is responsible for this dip in the amplitude. Here, we devise a fourth case with a corresponding parameter setting to illustrate that a similar dip occurs in 2D. The fourth case has the same settings as the third case, except that $\varepsilon_{\sqrt{2}} = 3D_s - \sqrt{3D_s(1 + 4\pi^2 \times 2/B)} = -0.2406$. That is, $(\varepsilon_{\sqrt{2}}, D_s)$ is on the lower branch of the marginal oscillation curve of the $\boldsymbol{q} = (1, 1)$ mode. Because the initial perturbation of u contains only this mode, we expect the evolution of the u profile to have a similar flip, which leads to a dip in the amplitude decay. The calculations confirm this behaviour in the 2D case. For example, the central region of u changes from high elevation at $t = 0.172$ to low elevation $u(x, y, t)$ at $t = 0.258$ [4]. Clearly the profile of u is flipped at some moment during this interval. Figure 17 shows a dip in the amplitude curve of u between $t = 0.172$ and 0.258. Thus this demonstrates that the similar mixed oscillatory-monotonic decay pattern exists in the 2D problem when (ε_q, D_s) is on the marginal oscillation curve of the qth mode.

The problem was also simulated on circular, triangular and trapezoidal domains using unstructured triangulations. Here we present results only for the circular domain. Recall that an unattenuated standing wave is developed on the unit square with the initial perturbation of wave vector $\boldsymbol{q} = (1, 1)$. The previous stability analysis for the square cannot be directly applied here. However, we anticipate that some qualitative approximation to a standing wave pattern may be exhibited for the other geometries considered. For example, such a pattern can be inferred from the profiles for u and Γ on the circular domain (Figures 19 and 20) as well as in the amplitude profiles after the initial transient (e.g. beyond $t \sim 0.2$ in Figure 18). Similar qualitative standing wave behaviour is observed for the equilateral triangle. For the trapezoid domain, because of the asymmetry in the geometry, the directions of the wave

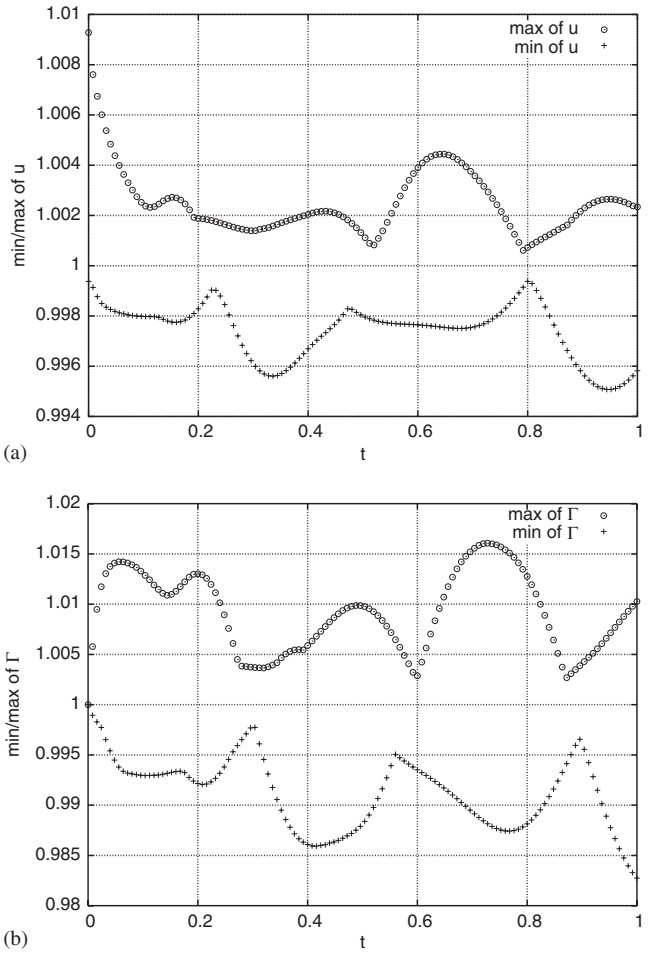

Figure 18. Min/max values of $u(x, y, t)$ and $\Gamma(x, y, t)$. Circle domain. $\varepsilon_1 = 0.16$. $\Delta t = 0.001$, $T = 1$: (a) min/max of u; and (b) min/max of Γ.

reflections are not as well aligned as the other cases. As a result, the standing wave pattern is less obvious [4].

4. CONCLUSIONS

In this study we have investigated the variational formulation, finite element approximation and solution strategy for the problem developed and analysed in Part I, which concerns long scale evolution of heated thin liquid films including the effect of a dilute surfactant monolayer. Numerical simulations are conducted on 1D and 2D domains. These solutions demonstrate several interesting interactions with respect to the stability of the surface elevation. For

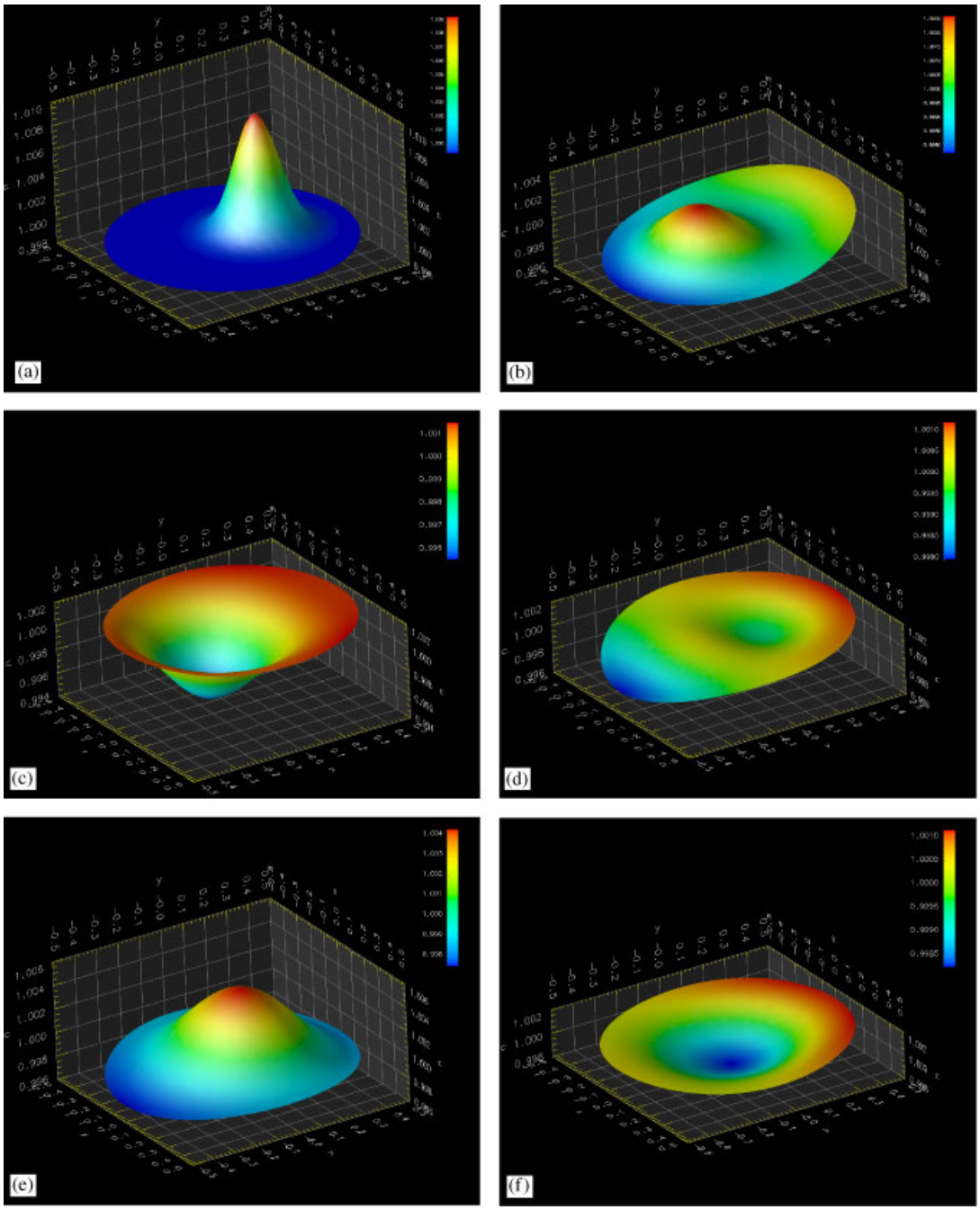

Figure 19. $u(x, y, t)$. Circle domain, centred at origin with radius 0.5. $\varepsilon_1 = 0.16$. $\Delta t = 0.001$, $T = 1$: (a) u at $t = 0$; (b) u at $t = 0.167$; (c) u at $t = 0.334$; (d) u at $t = 0.5$; (e) u at $t = 0.667$; and (f) u at $t = 0.834$.

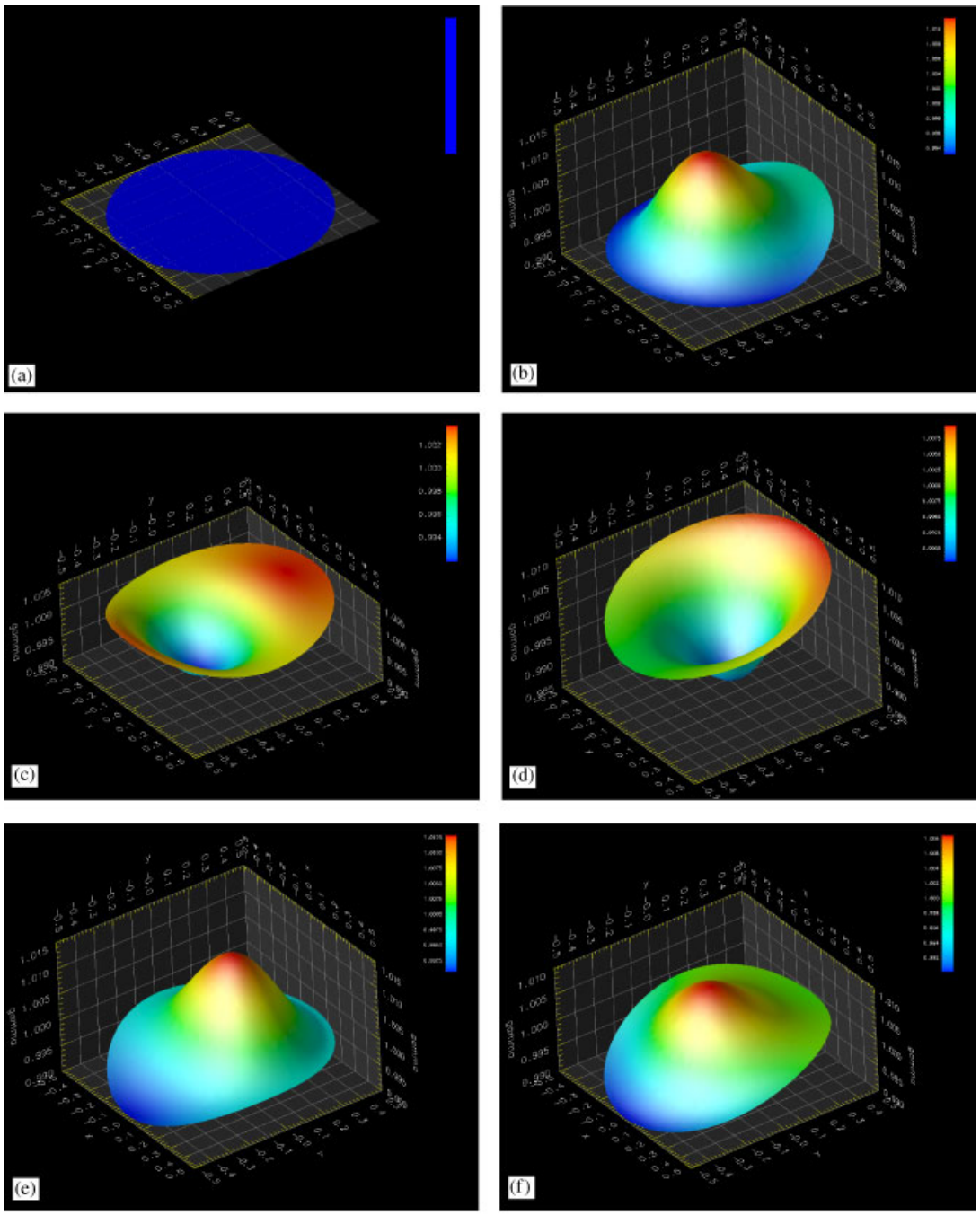

Figure 20. $\Gamma(x, y, t)$. Circle domain, centred at origin with radius 0.5. $\varepsilon_1 = 0.16$. $\Delta t = 0.001$, $T = 1$: (a) $\Gamma = 1$ at $t = 0$; (b) Γ at $t = 0.167$; (c) Γ at $t = 0.334$; (d) Γ at $t = 0.5$; (e) Γ at $t = 0.667$; and (f) Γ at $t = 0.834$.

instance, in the oscillatory parametric region, we observe the standing wave patterns and the characteristic parameters (e.g. period, phase difference, amplitude ratio and growth rate) obtained from the time dependent solutions agree reasonably with the linear stability analysis; in the non-oscillatory parametric region, we observe two different exponential growth rates as predicted by the linear stability analysis. We also observe from the numerical solutions some interesting non-linear features not predicted in the linear stability analysis. For example, the 'dip' in the decay curve of the envelope of the elevation in the marginal non-oscillatory case, the quick ramp up of the concentration at the initial phase in the non-oscillatory cases, and the non-zero minimum solution envelopes in the oscillatory cases.

There are several obvious areas for continued study such as extending the inclined plane treatment [3] to the full surfactant-thermocapillary problem, investigating the bifurcation behaviour in the inclined plane problem and in particular the Hopf bifurcation in the surfactant problem using weakly non-linear analysis, continuation and branch switching methods, developing a multi-scale model to include physics at both long wavelength scale in the outer region and the short capillary length scale in the inner region, and further improvement of the finite element formulations using high order bases. The extension to include surfactant effects in the inverted problem (where the fluid layer is adjacent to the upper plate and the gas is below so gravity is destabilizing and thermocapillarity is stabilizing) and the short wavelength instability problem in Bénard–Marangoni convection (the Hexagonal convection cells) are both of interest and would be natural extensions of the present work. For example, in the latter case, using a similar physical argument to that discussed in the present study, one would conjecture that the surfactant effect will delay the onset of instability in these problems as well.

ACKNOWLEDGEMENTS

We would like to extend our appreciation to Dr Van Nguyen for several very stimulating discussions on the behaviour and properties of monolayer surfactants and for providing several key references that were helpful in the present numerical modeling investigation.

REFERENCES

1. VanHook SJ, Schatz MF, Swift JB, McCormick WD, Swinney HL. Long-wavelength surface-tension-driven Bénard convection: experiment and theory. *Journal of Fluid Mechanics* 1997; **345**:45–78.
2. VanHook SJ. Long-wavelength instability in surface-tension-driven Bénard convection. *Ph.D. Dissertation*, University of Texas at Austin, 1996.
3. Wang X, Carey GF. Finite element study of a heated thin fluid layer. *Numerical Heat Transfer* 2004; **45**(9): 841–867.
4. Wang X, Carey GF. Finite element study of a heated thin fluid layer including surfactant effects. *ICES Report*, The University of Texas at Austin, 2003.
5. Eggleton CD, Tsai T, Stebe KJ. Tip streaming from a drop in the presence of surfactants. *Physics Review Letters* 2001; **87**(4):048302.
6. Eggleton CD, Pawar YP, Stebe KJ. Insoluble surfactants on a drop in an extensional flow: a generalization of the stagnated surface limit to deforming interfaces. *Journal of Fluid Mechanics* 1999; **385**:79–99.
7. *Handbook of Chemistry and Physics* (58th edn), 1977.

